CONDENSED MATTER PHYSICS

Subunit cell–level measurement of polarization in an individual polar vortex

Yuanwei Sun[1,2]*, Adeel Y. Abid[1,2]*, Congbing Tan[3]†, Chuanlai Ren[3], Mingqiang Li[1,2], Ning Li[1,2], Pan Chen[4], Yuehui Li[1,2], Jingmin Zhang[2], Xiangli Zhong[3‡], Jinbin Wang[3], Min Liao[3], Kaihui Liu[5,6], Xuedong Bai[4,6], Yichun Zhou[3], Dapeng Yu[5,6,7], Peng Gao[1,2,6‡]

Recently, several captivating topological structures of electric dipole moments (e.g., vortex, flux closure) have been reported in ferroelectrics with reduced size/dimensions. However, accurate polarization distribution of these topological ferroelectric structures has never been experimentally obtained. We precisely measure the polarization distribution of an individual ferroelectric vortex in $PbTiO_3/SrTiO_3$ superlattices at the subunit cell level by using the atomically resolved integrated differential phase contrast imaging in an aberration-corrected scanning transmission electron microscope. We find, in vortices, that out-of-plane polarization is larger than in-plane polarization, and that downward polarization is larger than upward polarization. The polarization magnitude is closely related to tetragonality. Moreover, the contribution of the Pb—O bond to total polarization is highly inhomogeneous in vortices. Our precise measurement at the subunit cell scale provides a sound foundation for mechanistic understanding of the structure and properties of a ferroelectric vortex and lattice-charge coupling phenomena in these topological ferroelectric structures.

INTRODUCTION

Novel and complex topological structures for electric polarization in nanostructure ferroelectrics have gained considerable attention in the recent past (1, 2) because of the growing interest in advanced memory storage (1, 3, 4) and the potential applications of such structures as a functional element in future nanoelectronics (5). With reduced size/dimensions in ferroelectric nanodots (6), nanowires (2), thin films (3, 5), and superlattices (2, 7, 8), the pronounced effects of boundary (surface and interface) drive the emergence of exotic configurations of electric dipole moments (9), such as the vortex-antivortex state (7, 10), polarization wave (11), and flux-closure domains (5, 12). In particular, the vortex-like polarization configuration with continuous rotation similar to vortex flow in fluid mechanics (13) and skyrmions in ferromagnetisms (rotational spin topologies) (14) can exist in ferroelectrics that are a few nanometers in size, mainly due to the large depolarizing field (1, 15) and/or strain (7, 11), which may be promising for data storage applications (4, 5). Within such a vortex state, the memory bits are considered to be stored with almost little intrabit cross-talk with adjacent bits on one hand (1), and on the other hand, this nanosized polarization state (vortex-antivortex) is believed to yield a high density of bits (1, 15). Theoretical studies have initially predicted the rotation of dipole vectors in ferroelectrics (1, 7, 15); subsequently, the inferred idea of dipole rotation was experimentally materialized in rhombohedral $BiFeO_3$ (3) and tetragonal $PbZr_{0.2}Ti_{0.8}O_3$ (5) thin films, as well as in ferroelectric/paraelectric superlattices

PbTiO₃/SrTiO₃ (8, 11, 16, 17). In this superlattice system, the observed long-range ordered arrays of vortices are believed because of a delicate balancing interplay among polarization gradient energy, electric energy, and elastic energy (10). Very recently, the measurements of electric field and polarization field in $(PbTiO_3)_{12}/(SrTiO_3)_{12}$ are reported by using an electron microscopy pixel array detector (18).

The rotatable and highly nonuniform spontaneous polarization configuration driven by the electrical and mechanical boundary conditions is essential for the emergent exotic properties of vortices. Thus, it is of prime importance to know the distribution of electric dipoles within an individual vortex for which the screening mechanism dominates its electrical activity. Although theoretical investigations [e.g., phase-field modeling (19)] have calculated the spatially distributed electric dipoles, experimental measurements are very challenging because of the small size of the vortex (~4 nm) and the largely spatial variety of polarization within a single vortex; e.g., polarization anisotropically changes from −44.81 to 44.81 μC cm⁻² in-plane and from −54.24 to 54.24 μC cm⁻² out-of-plane for the $(PbTiO_3)_{10}/(SrTiO_3)_{10}$ superlattice system, as predicted by the phase-field modeling (10). Most of the knowledge on the polarization orientation and magnitude of polar vortices in these superlattice systems (8, 10, 11, 20) was extracted from the high-angle annular dark-field (HAADF) imaging in aberration-corrected scanning transmission electron microscopy (STEM) by measuring the atomic displacement between Pb and Ti, mainly because the HAADF image with atomic number–dependent contrast is quite insensitive to the lighter oxygen atom (21). This method is based on a simple empirical relationship (22): $P_s = k\Delta d$, where P_s is the polarization, k is an empirical constant fitted from macroscopic measurement of many ferroelectric materials, and Δd is the displacement between the cations. Compared with the precise equation $P_s = \frac{1}{V}\sum\delta_i Z_i$ (23), where V is the volume of unit cell, δ is the displacement/shift of atom i from its centrosymmetric position, and Z is the Born effective charge of atom i calculated by ab initio theory (24), the above measurement based on the HAADF image omitting the oxygen positions is therefore unable to extract accurate information on polarization distribution. On the other hand, in the vortex region with a highly distorted lattice, it is impossible to deduce the

oxygen positions simply based on cationic configuration. Therefore, experimentally quantitative measurement of polarization in an individual polar vortex has not been achieved yet. To precisely extract unit cell–scale magnitude and orientation of polarization distribution in such a highly distorted structure, robustly imaging oxygen positions is a prime prerequisite.

Here, we characterize the vortex-antivortex configuration in a $(PbTiO_3)_{10}/(SrTiO_3)_{10}$ superlattice on a GdScO$_3$ substrate with a SrRuO$_3$ bottom electrode by using integrated differential phase contrast (iDPC) imaging in aberration-corrected STEM, which enables us to simultaneously visualize both heavier cations and relatively lighter oxygen columns (25, 26). On the basis of the atomically resolved iDPC images, we attained essential parameters such as bond length and atomic shift/displacement to quantitatively measure the magnitude and orientation of polarization at the subunit cell scale. Our results show that the polarization is highly nonuniform to continuously rotate the vortex structure. The polarization is changed from ~−50.8 to ~62.3 μC cm^{-2} for the in-plane (P_x) and ~−108.8 to ~88.3 μC cm^{-2} for the out-of-plane (P_z) passing the cores of the vortices, where the latter is typically larger than that of previous phase-field modeling (10). The magnitude of polarization is closely associated with tetragonality. For the out-of-plane component P_z, the upward polarization is smaller than the downward polarization, thus leading to a small net downward polarization in the superlattice film. At the sub-unit cell level, the contribution of P_{Pb-O} largely varies within a single vortex; i.e., in the downward domain, the Pb−O bond contributes more polarization than the Ti−O bond, while in the upward domain, Pb−O contributes less, indicating that the highly flexible Pb−O bond is the possible main origin of largely varied out-of-plane polarization. Note that the precise measurement of polarization and sub-unit cell–level information cannot be obtained from the measurements that omit oxygen information such as HAADF. The accurate measurement of polarization in a single ferroelectric vortex in this study is helpful for the mechanistic understanding of lattice-charge coupling phenomena such as ferroelectricity, piezoelectricity, and flexo-electricity at the nanoscale.

RESULTS

Vortex in superlattice

Superlattice thin films $(PbTiO_3)_n/(SrTiO_3)_n$ (where n is the thickness of each PbTiO$_3$ and SrTiO$_3$ layer in terms of unit cell), which contain vortex arrays and flux-closure domain patterns (10, 12, 16, 17), are grown on the GdScO$_3$ (110) substrate with the SrRuO$_3$ substrate by pulsed laser deposition (PLD). Experimental details are shown in the Supplementary Materials. The low-magnification STEM image of $(PbTiO_3)_{10}/(SrTiO_3)_{10}$ in Fig. 1A depicts an alternative PbTiO$_3$ layer with bright contrast and an SrTiO$_3$ layer with dark contrast.
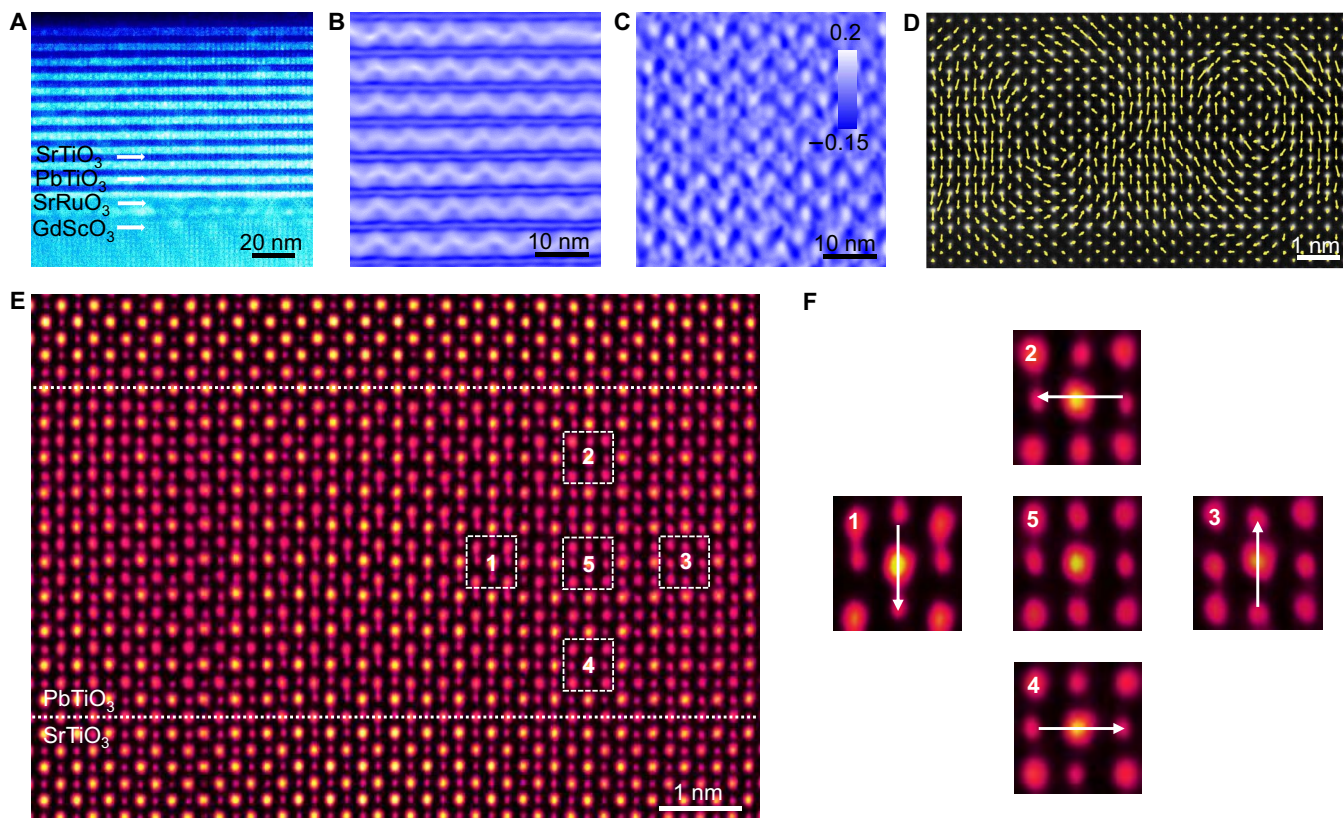

Fig. 1. Structural characterization of (SrTiO$_3$)$_{10}$/(PbTiO$_3$)$_{10}$ superlattices. (A) Low-magnification STEM image of (PbTiO$_3$)$_{10}$/(SrTiO$_3$)$_{10}$ with the zone axis [010] of PbTiO$_3$. (B) Out-of-plane strain ε_{yy} and (C) in-plane strain ε_{xx} calculated from GPA based on a STEM image. (D) High-angle annular dark-field (HAADF) STEM image overlapped with the polar vectors of a single vortex-antivortex pair in the PbTiO$_3$ layer sandwiched between two SrTiO$_3$ layers, showing a continuous rotation of electric dipole vectors. (E) Atomically resolved iDPC image with inverted contrast for clarity of purpose. (F) Five enlarged unit cells (left, right, top, bottom, and middle) are portrayed to depict the direction of polarization based on the atomic displacement of oxygen with respect to the cations.

Figure 1 (B and C) shows geometric phase analysis (GPA) maps of the superlattice sample (see more details in fig. S1). The white-colored sinusoidal wavelike pattern along the [100] direction suggests the long-range ordering of vortex (clockwise) and antivortex (anticlockwise) arrays, whereas no such feature can be seen in $SrTiO_3$ layers. The sharpness and coherency of the interface in $PbTiO_3/SrTiO_3$ multilayers can be visualized in an atomically resolved HAADF polar map (Fig. 1D) (11), wherein two tail-to-tail sets of in-plane polarization are bifurcated by out-of-plane polarization, thus making the adjacent pairs of vortex and antivortex similar to previous studies. From the iDPC image for a pair of vortices in Fig. 1E (colored for clarity), the atomic shift between cations and anions with respect to their respective centrosymmetric positions is visible to the naked eye, and such a shift between cations and an O atom seems more pronounced than that between Pb and Ti (Fig. 1F). Thus, the iDPC image not only presents the information of oxygen configurations within the highly distorted vortex but also should give much better accuracy for polarization measurements that are based on the displacements between cations and oxygen.

Precise measurement of polarization

On the basis of this iDPC image, the bond length and atomic displacement/shift variation within the vortex-antivortex, both in-plane and out-of-plane, of cation-anion (calculated from the complete atomic positions including the lighter oxygen) are incorporated in the Supplementary Materials (see details in fig. S2), whereas Fig. 2A depicts the nonuniform distribution of displacement vectors (as well as polarization) of the vortex-antivortex pair. Figure 2 (B and C) shows color maps portraying the unit cell–level distribution of polarization, both out-of-plane (along [001]) and in-plane (means parallel to the interface), respectively, for the iDPC image in fig. S3A, while fig. S3B depicts the total polarization magnitude. Meanwhile, see Materials and Methods for details on the performed measurement. The line profiles in Fig. 2 (D and E) depict the polarization variation for both out-of-plane (horizontal outlines "a" and "b" in Fig. 2B) and in-plane (vertical outlines "c" and "d" drawing through interface-core-interface in Fig. 2C), respectively. The out-of-plane polarization P_z ~–108.8 to 88.3 μC cm^{-2} (Fig. 2D) exists between the vortex and the antivortex (in Fig. 2B), while the in-plane polarization P_x ~–50.8 to 62.3 μC cm^{-2} (Fig. 2E) occurs in the region between the core and the interface of $SrTiO_3$ and $PbTiO_3$. Figure 2F shows the distribution of magnitude of the polarization for out-of-plane and in-plane in the $PbTiO_3$ layer having vortex configuration. The larger maximum P_z than P_x is representative of both experiment and phase-field modeling (10) owing to the compressive strain in this superlattice system. For comparison, the polarization of a single-layer $PbTiO_3$ film with thickness ~100 nm on the $SrTiO_3$ substrate is also measured to be ~94.6 μC cm^{-2} (fig. S4).

The previous phase-field modeling entails that in-plane P_x and out-of-plane P_z polarization distribution ranges are from –44.81 to 44.81 μC cm^{-2} and from –54.24 to 54.24 μC cm^{-2}, respectively, for the vortex in the $(PbTiO_3)_{10}/(SrTiO_3)_{10}$ superlattice having the same thickness as and with a similar substrate to our current work, with the polarization of bulk $PbTiO_3$ being set to 75 μC cm^{-2} (10). Therefore, this unit cell–level measurement of P_x is in good agreement with the phase-field simulation (50.8/94.6 < 44.81/75 < 62.3/94.6), while the measured P_z is larger than the expected value (88.3/94.6 > 54.24/75).

Both out-of-plane and in-plane lattice variation along with the tetragonality (c/a ratio is always larger than 1) maps are separately illustrated in Fig. 3. The contour outlines in Fig. 3C highlight those

regions where P_z is larger than 50 μC cm^{-2}; besides, the tetragonality is also typically larger, indicating that the magnitude of polarization is closely related to the tetragonality similar to other ferroelectric systems (27). Furthermore, according to recent reports, the flexoelectric effect seems to play a noticeable role in determining magnitude of polarization (20, 28) in a complicated manner. In contrast, the quantitative methodology carried out here by mapping the essential parameters of bond lengths and atomic displacements between cation and anion to determine the magnitude of polarization (23) can be considered far accurate, particularly when handling the complicated configuration patterns.

Moreover, the downward polarization is larger than the upward polarization, i.e., 108.8 μC cm^{-2} for downward polarization and 88.3 μC cm^{-2} for upward polarization, from the measurements in Fig. 3D, leading to a small net downward polarization in the superlattice. This may be understood by the polarization screening mechanism at the bottom electrode and/or top surface. Previous studies reported that the as-grown tetragonal $PbZr_{0.2}Ti_{0.8}O_3$ (29) and $PbTiO_3$ (30) on the $SrRuO_3$ electrode have downward polarization, because $SrRuO_3$ can effectively compensate for the negative bound charge at the interface.

Decoupling the contributions of Ti−O and Pb−O bonds

Another substantial aspect for these topological configurations having nonuniform polarization such as vortex-antivortex arrays is essentially correlated to subunit cell–level information (see also fig. S2), which cannot be extracted from the phase-field modeling, not to mention other experimental investigations. Color magnitude maps of out-of-plane polarization (P_z) obtained separately for SrO/PbO atomic planes/layers and TiO_2 atomic planes are shown in Fig. 4 (A and B, respectively), whereas magnitude maps of in-plane polarization (P_x) are illustrated in Fig. 4D (SrO/PbO atomic planes) and Fig. 4E (TiO_2 atomic planes). The ratio of polarization distribution maps of out-of-plane (P_z) and in-plane (P_x) polarization obtained separately for SrO/PbO atomic planes/layers and TiO_2 atomic planes is illustrated in Fig. 4 (C and F, respectively). Magnitude maps in Fig. 4 depict that, unlike the constant contribution of P_{TiO2} and P_{PbO} in bulk, both in-plane and out-of-plane contributions of Ti−O and Pb−O change over the entire vortex. The contribution of TiO_2 and PbO layers to the total polarization is not identical and was rather found to be largely inhomogeneous. For instance, for out-of-plane polarization distribution, the relative contribution is very different between the upward and downward domains from Fig. 4 (G and H); i.e., in the downward domain with larger polarization, the contribution of the Pb−O bond is pronounced compared to the Ti−O bond, while in the upward domain with smaller polarization, the contribution of the Pb−O bond becomes suppressed, indicating that the adjustable Pb−O bond is the main origin of largely varied polarization, which is probably because the Pb−O bonds, instead of being pure ionic, are partially covalent in nature, owing to the hybridization of Pb 6s and O 2p orbitals; as a result, coulomb interactions account for the highly heterogeneous ferroelectric distortions (31), which were also observed in other lead-based ferroelectrics (29). Furthermore, the hybridized Pb and O states introduce the large strain, which, in turn, stabilizes the tetragonal ferroelectric phase. Thus, the altering trend of Pb−O bond length at different regions within the vortices is largely responsible for polarization variation. In contrast, although the ratio of in-plane polarization distribution in Fig. 4F also shows spatial fluctuation over the entire vortex, no clear trend is observed.
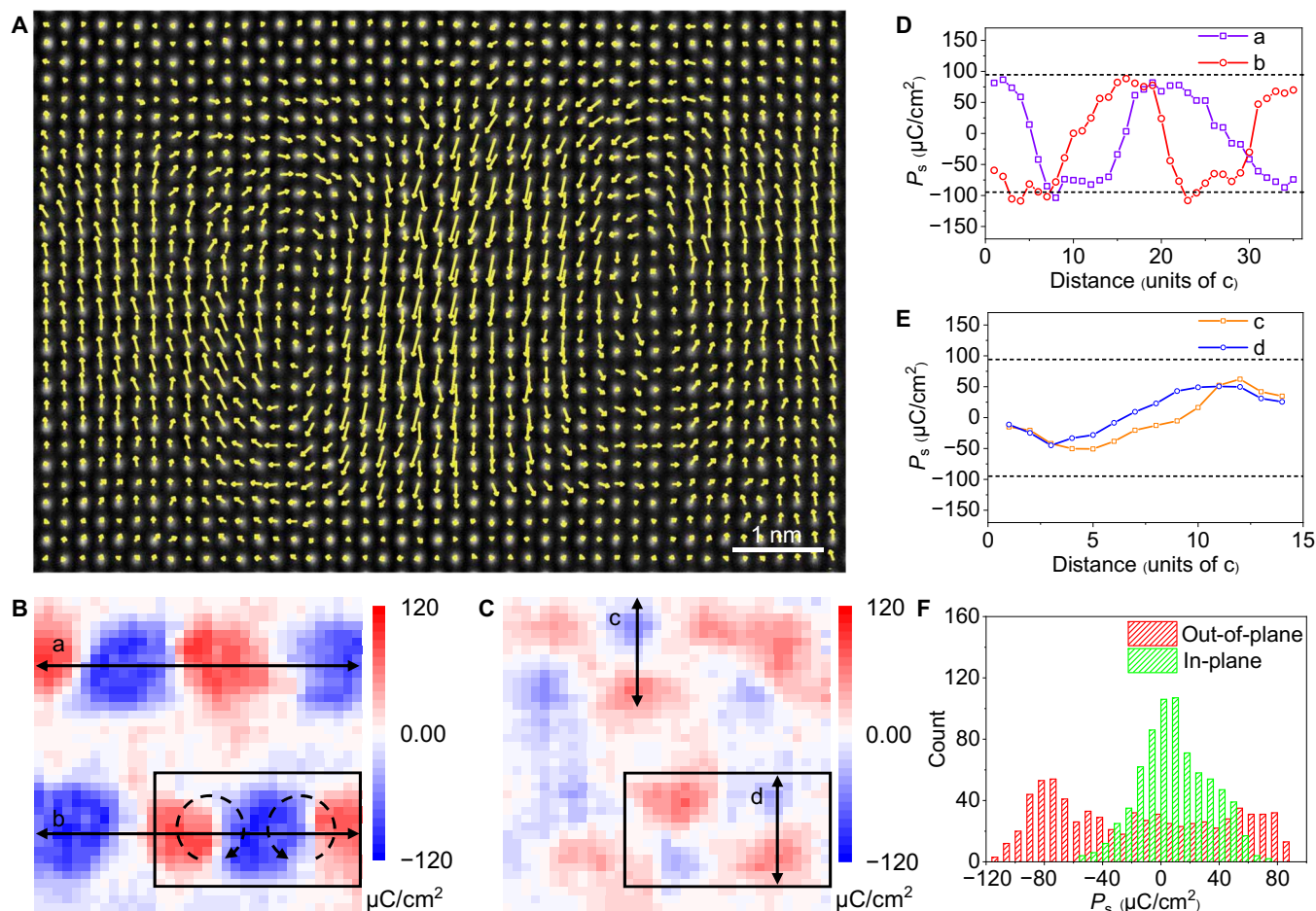
Fig. 2. Quantitative measurements of polarization distribution for a single vortex-antivortex pair based on the cation-anion atomic positions in the iDPC image. (**A**) An iDPC image overlapped with the polarization vectors that are calculated from the displacements between cations and anions. The unit cell–mapped (**B**) out-of-plane (P_z) and (**C**) in-plane (P_x). The plot of polarization for (**D**) the horizontally marked outline region in (B) and the vertically traced outline region in (C). Black dashed lines in (D) and (E) denote the bulk value of polarization. (**F**) Distribution of magnitude of polarization for out-of-plane and in-plane in PbTiO$_3$ layer having vortex configuration.

DISCUSSION

Onward, we compare our measurements on cation-anion configuration from an iDPC image (see Fig. 2) with those from an HAADF image (fig. S5) in which the information of oxygen positions is omitted. Although the HAADF image can also produce a similar pattern of polarization distribution (fig. S5, B and C) to that of iDPC, there are a few differences between them. First, from the HAADF image, the estimated polarization P_x is ~−39.4 to 40.2 µC cm^{-2} and P_z is ~−69.6 to 62.9 µC cm^{-2}, and the latter is considerably smaller than that from the iDPC image in Fig. 2. Second, the subunit cell information (i.e., the relative contribution of PbO and TiO$_2$ planes) is inaccessible from the HAADF image. Therefore, to precisely measure the polarization distribution in a highly structural distorted vortex, oxygen information is necessary.

Next, we discuss the applicability and limitations of the atomic-scale measurements from the iDPC image. The error of displacement measurement mainly comes from the optical misalignments (e.g., specimen mistilt and residual lens aberration) and the structure inhomogeneity along the electron beam traveling direction. The former can be minimized by careful alignment, optimized imaging conditions

(e.g., choosing large convergence angle), and postcorrection during data analysis, while the latter depends on the sample itself. For example, in fig. S6, the displacements in a cubic SrTiO$_3$ are measured to be 3.2 ± 2.0 pm between Sr and O and 4.0 ± 1.9 pm between TiO and O, corresponding to 9.1 ± 3.8 µC cm^{-2} in total polarization, which can be considered as the error level for measurements based on iDPC for our sample and under the typical experimental conditions shown in the Supplementary Materials. The mean values (e.g., 3.2 and 4 pm) mainly represent the effects of misalignments and residual lens aberration, while the SD (2.0 and 1.9 pm) mainly comes from the structural inhomogeneity. Both of them account for the error bars and limit measurement precision. In principle, for those material systems with displacements above the error level, polarization measurement at the subunit cell level is practicable (see more detailed discussion in the Supplementary Materials).

Note that the measurement precision becomes worse for those specimens with large structural inhomogeneity along the electron beam traveling direction, as the iDPC can only provide two-dimensional projected information identical to other images in TEM. To overcome this problem, atomically resolved three-dimensional imaging (*32*) is
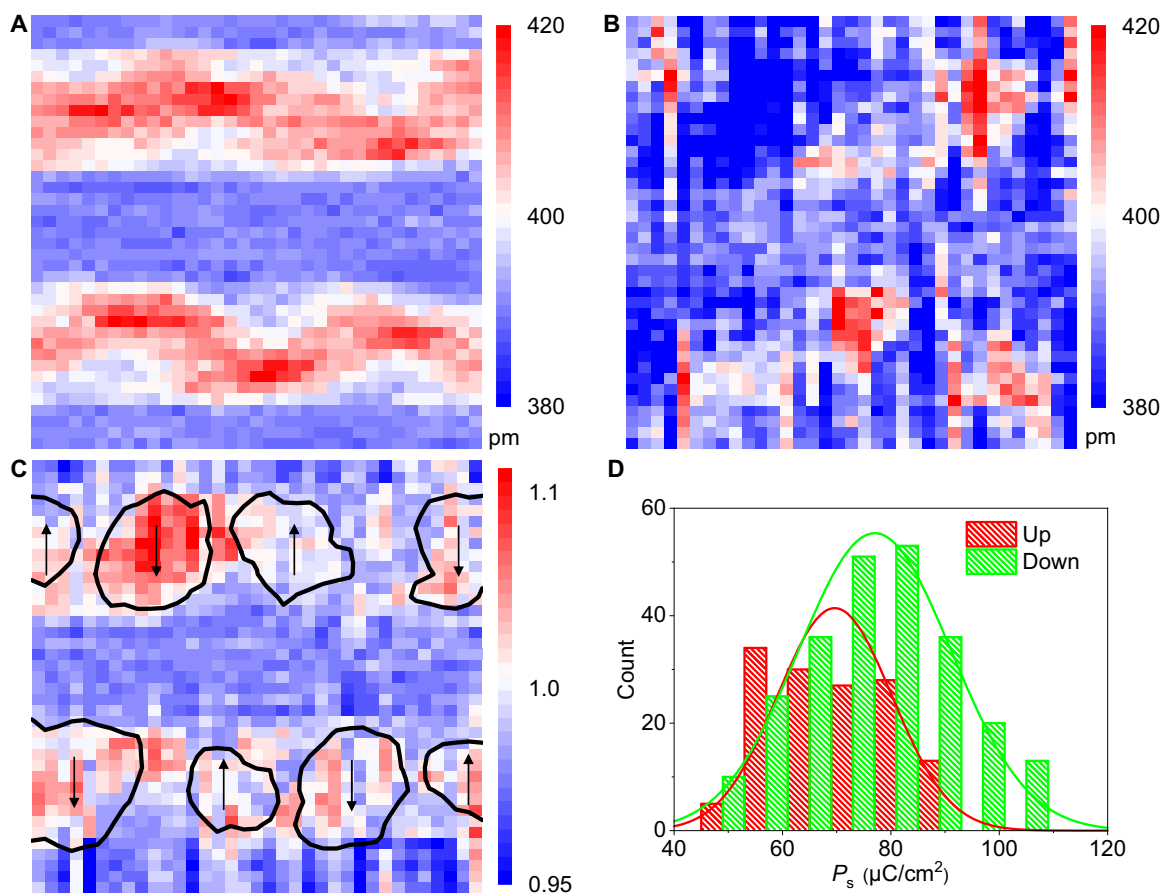
Fig. 3. Quantitative analysis of the out-of-plane and in-plane lattice constant along with calculation of tetragonality for the PbTiO₃/SrTiO₃ superlattice. Color magnitude map for lattice constant (**A**) out-of-plane and (**B**) in-plane. (**C**) Illustration of magnitude mapping for tetragonality (c/a ratio). The consecutive marked regions (in Fig. 2C) indicate upward (away from substrate) and downward (toward substrate) polarization (>50 μC cm⁻²). (**D**) Distribution of magnitude of polarization for upward (red data) and downward (green data) directed polar vectors in the PbTiO₃ layer having vortex configuration. The average value for downward (green data) and upward (red data) polarization magnitude is ~77.0 and ~69.6 μC cm⁻², respectively.
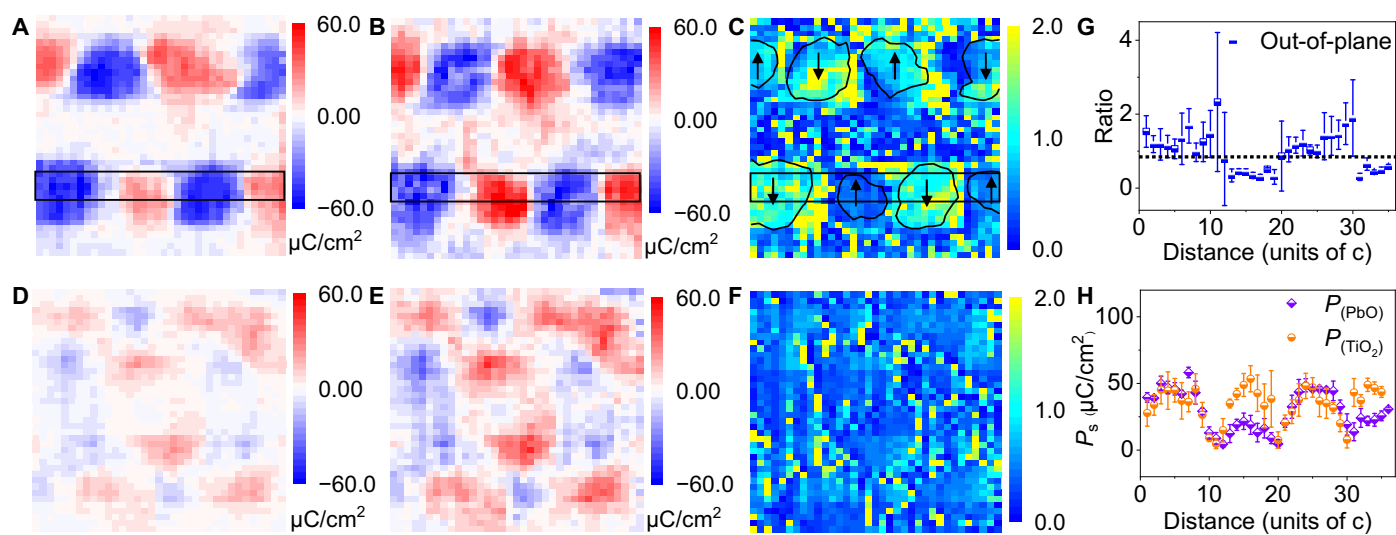
Fig. 4. Subunit scale level of polarization distribution. Color magnitude map of out-of-plane (P_z) polarization distribution obtained separately for (**A**) SrO/PbO atomic planes, (**B**) TiO₂ atomic planes, and (**C**) contribution ratio of $P_{(SrO/PbO)}$ to $P_{(TiO2)}$. Color magnitude map of in-plane (P_x) polarization distribution obtained separately for (**D**) SrO/PbO atomic planes, (**E**) TiO₂ atomic planes, and (**F**) contribution ratio of $P_{(SrO/PbO)}$ to $P_{(TiO2)}$. (**G**) Plot for the horizontally marked rectangular region in (C). (**H**) Plot for the horizontally marked rectangular regions in (A) and (B), at both PbO atomic planes (purple data) and TiO₂ atomic planes (orange data).

needed in the future. Nevertheless, in our study, the vortex tube is straight and uniform over a few hundreds of nanometers along the [010] direction (10), and the previous density functional theory (28) calculation and three-dimensional phase-field simulation (10) suggested that the polarization has only two components, P_z (out-of-plane) and P_x (in-plane), with no polarization along the electron beam direction (labeled y); therefore, the two-dimensional projected iDPC image can still provide key information on polarization distribution.

In summary, we use the iDPC imaging technique to accurately measure the atomic structure and polarization distribution of an individual ferroelectric vortex in the PbTiO$_3$/SrTiO$_3$ superlattice system. Our study shows that magnitude of polarization is nonuniform and that the out-of-plane polarization P_z ~−108.8 to 88.3 μC cm^{-2} exists between the vortex and the antivortex and the in-plane polarization P_x ~−50.8 to 62.3 μC cm^{-2} occurs in the region between the core and the interface of SrTiO$_3$ and PbTiO$_3$. The measured in-plane polarization P_x is in good agreement with the previous phase-field simulation, while the out-of-plane P_z is typically larger than the expected value. Furthermore, for the out-of-plane P_z, the downward polarization is larger than the upward polarization. At the subunit cell level, the contribution of Pb—O to the total out-of-plane polarization P_z is very prominent in the downward domain, while less significant in the upward domain, indicating that compared to the Ti—O bond, the flexible Pb—O bond is the main origin of largely varied polarization in the vortex. A comparative investigation further clarifies that, although the direction of polar vectors can also be obtained by the measurements of the displacements between cations, the precise magnitude of polarization must require the oxygen information. The accurate measurement of polarization of a single ferroelectric vortex is helpful for the mechanistic understanding of the properties of a polar vortex and lattice-charge coupling phenomena in these complex topological structures.

MATERIALS AND METHODS

Preparation of (PbTiO$_3$)$_{10}$/(SrTiO$_3$)$_{10}$ superlattices
Superlattices of (PbTiO$_3$)$_{10}$/(SrTiO$_3$)$_{10}$ were deposited on ~12 nm SrRuO$_3$-buffered, (110)-GdScO$_3$ substrates in a PLD system (PVD-5000) equipped with a krypton fluoride laser excimer laser (λ = 248 nm). Ceramic targets of SrRuO$_3$, SrTiO$_3$, and Pb$_{1.1}$TiO$_3$ (10 mol% excessive amount of lead to compensate for the evaporation loss of Pb) were used for the PLD deposition of the bottom electrode and the (PbTiO$_3$)$_{10}$/(SrTiO$_3$)$_{10}$ superlattices. The SrRuO$_3$ and superlattices were grown under a laser energy of 390 and 340 mJ per pulse, respectively, and at a pulse repetition rate of 10 Hz. The SrRuO$_3$ was firstly deposited at 690°C under an 80-mtorr oxygen pressure, and then the substrate was cooled down to 600°C for the subsequent growth of the (PbTiO$_3$)$_{10}$/(SrTiO$_3$)$_{10}$ superlattices. The growth temperature and oxygen pressure for the growth of the superlattices were 600°C and 200 mtorr, respectively. By controlling the growth time, thicknesses of the SrRuO$_3$, PbTiO$_3$, and SrTiO$_3$ layers were held at ~12, ~4, and ~4 nm, respectively. Immediately after the growth of the (PbTiO$_3$)$_{10}$/(SrTiO$_3$)$_{10}$ superlattices, the samples were cooled down to room temperature under a 200-mtorr oxygen pressure.

TEM sample preparation
For iDPC image acquisition, the cross-sectional TEM specimens were thinned to less than ~30 μm first by using mechanical polishing and then by performing argon ion milling. The ion-beam milling was

carried out using the Precision Ion Polishing System (Model 691, Gatan Inc.) with an accelerating voltage of 3.5 kV until a hole was made. Low voltage milling was performed with an accelerating voltage of 0.3 kV to remove the surface amorphous layer and to minimize damage.

Image acquisition and analysis
HAADF and iDPC images were recorded at 300 kV, using an aberration-corrected FEI Titan Themis G2 with spatial resolutions up to 60 pm. The convergence semi-angle for imaging is 30 mrad, and the collection semi-angle snap is 4 to 21 mrad for the iDPC imaging and 39 to 200 mrad for the HAADF. The iDPC and HAADF images are not from the same region, as they require different camera lengths and a slight change in focus and lens aberrations. The atom positions were determined by simultaneously fitting two-dimensional Gaussian peaks to an a priori perovskite unit cell using a MATLAB code (3). In brief, to attain proper atomic position, we used Microsoft Excel to sort the as-obtained random data first by x and then by y. Bond length is the distance between two adjacent atomic positions, for instance, m and $m + 1$, and we calculated it by using the basic distance formula $d = \sqrt{(x_2 - x_1)^2 + (y_2 - y_1)^2}$, where x_1, y_1 and x_2, y_2 are the coordinates of the mth and $(m + 1)$th atomic positions, respectively. Subsequently, a similar procedure was adopted for all rows (in-plane) and columns (out-of-plane). Lattice constant, both in-plane [100] and out-of-plane [001], is obtained by merely adding two adjacent bond lengths. Bond length data were further used to find the relative atomic displacement of atoms by using the numerical differentiation method through the formula $\frac{|d_{i+1} - d_i|}{2}$ (where d_i and d_{i+1} are the adjacent bond lengths). Eventually, we used these obtained data of displacement along with magnitude of electronic charge (e), volume of unit cell (a^2c), and Born effective charge values for Sr, Pb, and Ti to calculate polarization by using the following precise relationship: $P_s = \frac{1}{V}\sum \delta_i Z_i$ (23), where V is the volume of unit cell (it is a^2c in our case), δ is the displacement/shift of atom i from its centrosymmetric position, and Z is the Born effective charge of atom i calculated by ab initio theory having a numerical value of 7.12 for Ti, 3.9 for Pb, and 2.54 for Sr (24). The abovementioned method was used to attain the polarization for cation-anion (fully structured including the position of the lighter oxygen atom) configuration in the iDPC image. For polarization calculation based on the HAADF image, we used the atomic displacement between A and B sites (only based on cationic positions), and the procedure was based on the empirical formula (22) $P_s = k\Delta d$, where P_s is polarization, k is an empirical constant fitted from the macroscopic measurement of many ferroelectric materials, and Δd is the displacement between cations.

SUPPLEMENTARY MATERIALS
Supplementary material for this article is available at http://advances.sciencemag.org/cgi/content/full/5/11/eaav4355/DC1

Fig. S1. GPA of PbTiO$_3$/SrTiO$_3$ superlattices.
Fig. S2. Bond length analysis for polar vortex.
Fig. S3. An iDPC image of (SrTiO$_3$)$_{10}$/(PbTiO$_3$)$_{10}$ superlattices with illustrated PbTiO$_3$ and SrTiO$_3$ layers.
Fig. S4. Atomically resolved iDPC images of PbTiO$_3$/SrTiO$_3$ thin films.
Fig. S5. Polarization measurement based on cation-cation atomic positions in the HAADF image.
Fig. S6. Quantification of polarization distribution for PbTiO$_3$/SrTiO$_3$ thin films based on the cation-anion atomic positions in the iDPC image.
References (33–38)

REFERENCES AND NOTES

1. I. I. Naumov, L. Bellaiche, H. Fu, Unusual phase transitions in ferroelectric nanodisks and nanorods. *Nature* **432**, 737–740 (2004).

2. W. J. Chen, Y. Zheng, B. Wang, Large and tunable polar-toroidal coupling in ferroelectric composite nanowires toward superior electromechanical responses. *Sci. Rep.* **5**, 11165 (2015).

3. C. T. Nelson, B. Winchester, Y. Zhang, S.-J. Kim, A. Melville, C. Adamo, C. M. Folkman, S.-H. Baek, C.-B. Eom, D. G. Schlom, L.-Q. Chen, X. Q. Pan, Spontaneous vortex nanodomain arrays at ferroelectric heterointerfaces. *Nano Lett.* **11**, 828–834 (2011).

4. J. F. Scott, Applications of modern ferroelectrics. *Science* **315**, 954–959 (2007).

5. C.-L. Jia, K. W. Urban, M. Alexe, D. Hesse, I. Vrejoiu, Direct observation of continuous electric dipole rotation in flux-closure domains in ferroelectric Pb(Zr,Ti)O₃. *Science* **331**, 1420–1423 (2011).

6. A. Schilling, D. Byrne, G. Catalan, K. G. Webber, Y. A. Genenko, G. S. Wu, J. F. Scott, J. M. Gregg, Domains in ferroelectric nanodots. *Nano Lett.* **9**, 3359–3364 (2009).

7. Z. Jiang, B. Xu, F. Li, D. Wang, C.-L. Jia, Electric dipole sheets in BaTiO₃/BaZrO₃ superlattices. *Phys. Rev. B* **91**, 014105 (2015).

8. G.-Y. Kim, K. Chu, K.-D. Sung, H.-S. Lee, S.-D. Kim, K. Song, T. Choi, J. Lee, J. P. Buban, S.-Y. Yoon, K.-H. Kim, C.-H. Yang, S.-Y. Choi, Disordered ferroelectricity in the PbTiO₃/SrTiO₃ superlattice thin film. *APL Mater.* **5**, 066104 (2017).

9. S. V. Kalinin, D. A. Bonnell, Imaging mechanism of piezoresponse force microscopy of ferroelectric surfaces. *Phys. Rev. B* **65**, 125408 (2002).

10. A. K. Yadav, C. T. Nelson, S. L. Hsu, Z. Hong, J. D. Clarkson, C. M. Schlepütz, A. R. Damodaran, P. Shafer, E. Arenholz, L. R. Dedon, D. Chen, A. Vishwanath, A. M. Minor, L. Q. Chen, J. F. Scott, L. W. Martin, R. Ramesh, Observation of polar vortices in oxide superlattices. *Nature* **530**, 198–201 (2016).

11. L. Lu, Y. Nahas, M. Liu, H. C. Du, Z. J. Jiang, S. P. Ren, D. W. Wang, L. Jin, S. Prokhorenko, C.-L. Jia, L. Bellaiche, Topological defects with distinct dipole configurations in PbTiO₃/SrTiO₃ multilayer films. *Phys. Rev. Lett.* **120**, 177601 (2018).

12. Y. L. Tang, Y. L. Zhu, X. L. Ma, A. Y. Borisevich, A. N. Morozovska, E. A. Eliseev, W. Y. Wang, Y. J. Wang, Y. B. Xu, Z. D. Zhang, S. J. Pennycook, Observation of a periodic array of flux-closure quadrants in strained ferroelectric PbTiO₃ films. *Science* **348**, 547–551 (2015).

13. J. Jeong, F. Hussain, On the identification of a vortex. *J. Fluid Mech.* **285**, 69–94 (1995).

14. N. Nagaosa, Y. Tokura, Topological properties and dynamics of magnetic skyrmions. *Nat. Nanotech.* **8**, 899–911 (2013).

15. I. Naumov, A. M. Bratkovsky, Unusual polarization patterns in flat epitaxial ferroelectric nanoparticles. *Phys. Rev. Lett.* **101**, 107601 (2008).

16. P. Shafer, P. García-Fernández, P. Aguado-Puente, A. R. Damodaran, A. K. Yadav, C. T. Nelson, S.-L. Hsu, J. C. Wojdeł, J. Íñiguez, L. W. Martin, E. Arenholz, J. Junquera, R. Ramesh, Emergent chirality in the electric polarization texture of titanate superlattices. *Proc. Natl. Acad. Sci. U.S.A.* **115**, 915–920 (2018).

17. Z. J. Hong, A. R. Damodaran, F. Xue, S.-L. Hsu, J. Britson, A. K. Yadav, C. T. Nelson, J.-J. Wang, J. F. Scott, L. W. Martin, R. Ramesh, L. Q. Chen, Stability of polar vortex lattice in ferroelectric superlattices. *Nano Lett.* **17**, 2246–2252 (2017).

18. A. K. Yadav, K. X. Nguyen, Z. J. Hong, P. García-Fernández, P. Aguado-Puente, C. T. Nelson, S. Das, B. Prasad, D. Kwon, S. Cheema, A. I. Khan, C. M. Hu, J. Íñiguez, J. Junquera, L.-Q. Chen, D. A. Muller, R. Ramesh, S. Salahuddin, Spatially resolved steady-state negative capacitance. *Nature* **565**, 468–471 (2019).

19. P. Wu, X. Ma, Y. Li, V. Gopalan, L.-Q. Chen, Dipole spring ferroelectrics in superlattice SrTiO₃/BaTiO₃ thin films exhibiting constricted hysteresis loops. *Appl. Phys. Lett.* **100**, 092905 (2012).

20. A. R. Damodaran, J. D. Clarkson, Z. Hong, H. Liu, A. K. Yadav, C. T. Nelson, S.-L. Hsu, M. R. McCarter, K.-D. Park, V. Kravtsov, A. Farhan, Y. Dong, Z. Cai, H. Zhou, P. Aguado-Puente, P. García-Fernández, J. Íñiguez, J. Junquera, A. Scholl, M. B. Raschke, L.-Q. Chen, D. D. Fong, R. Ramesh, L. W. Martin, Phase coexistence and electric-field control of toroidal order in oxide superlattices. *Nat. Mater.* **16**, 1003–1009 (2017).

21. K. Takehara, Y. Sato, T. Tohei, N. Shibata, Y. Ikuhara, Titanium enrichment and strontium depletion near edge dislocation in strontium titanate [001]/(110) low-angle tilt grain boundary. *J. Mater. Sci.* **49**, 3962–3969 (2014).

22. S. C. Abrahams, S. K. Kurtz, P. B. Jamieson, Atomic displacement relationship to curie temperature and spontaneous polarization in displacive ferroelectrics. *Phys. Rev.* **172**, 551–553 (1968).

23. C.-L. Jia, V. Nagarajan, J.-Q. He, L. Houben, T. Zhao, R. Ramesh, K. Urban, R. Waser, Unit-cell scale mapping of ferroelectricity and tetragonality in epitaxial ultrathin ferroelectric films. *Nat. Mater.* **6**, 64–69 (2007).

24. W. Zhong, R. D. King-Smith, D. Vanderbilt, Giant LO-TO splittings in perovskite ferroelectrics. *Phys. Rev. Lett.* **72**, 3618–3621 (1994).

25. I. Lazić, E. G. T. Bosch, S. Lazar, Phase contrast STEM for thin samples: Integrated differential phase contrast. *Ultramicroscopy* **160**, 265–280 (2016).

26. E. Yücelen, I. Lazić, E. G. T. Bosch, Phase contrast scanning transmission electron microscopy imaging of light and heavy atoms at the limit of contrast and resolution. *Sci. Rep.* **8**, 2676 (2018).

27. J. X. Zhang, Q. He, M. Trassin, W. Luo, D. Yi, M. D. Rossell, P. Yu, L. You, C. H. Wang, C. Y. Kuo, J. T. Heron, Z. Hu, R. J. Zeches, H. J. Lin, A. Tanaka, C. T. Chen, L. H. Tjeng, Y.-H. Chu, R. Ramesh, Microscopic origin of the giant ferroelectric polarization in tetragonal-like BiFeO₃. *Phys. Rev. Lett.* **107**, 147602 (2011).

28. P. Aguado-Puente, J. Junquera, Structural and energetic properties of domains in PbTiO₃/SrTiO₃ superlattices from first principles. *Phys. Rev. B* **85**, 184105 (2012).

29. P. Gao, Z. Y. Zhang, M. Q. Li, R. Ishikawa, B. Feng, H.-J. Liu, Y.-L. Huang, N. Shibata, X. M. Ma, S. L. Chen, J. M. Zhang, K. H. Liu, E.-G. Wang, D. P. Yu, L. Liao, Y.-H. Chu, Y. C. Ikuhara, Possible absence of critical thickness and size effect in ultrathin perovskite ferroelectric films. *Nat. Commun.* **8**, 15549 (2017).

30. M. Q. Li, B. Wang, H.-J. Liu, Y.-L. Huang, J. M. Zhang, X. M. Ma, K. H. Liu, D. P. Yu, Y.-H. Chu, L.-Q. Chen, P. Gao, Direct observation of weakened interface clamping effect enabled ferroelastic domain switching. *Acta Mater.* **171**, 184–189 (2019).

31. R. E. Cohen, Origin of ferroelectricity in perovskite oxides. *Nature* **358**, 136–138 (1992).

32. J. Miao, P. Ercius, S. J. Billinge, Atomic electron tomography: 3D structures without crystals. *Science* **353**, 2257–2251 (2016).

33. P. Gao, A. Kumamoto, R. Ishikawa, N. Lugg, N. Shibata, Y. C. Ikuhara, Picometer-scale atom position analysis in annular bright-field STEM imaging. *Ultramicroscopy* **184**, 177–187 (2018).

34. S. E. Maccagnano-Zacher, K. A. Mkhoyan, E. J. Kirkland, J. Silcox, Effects of tilt on high-resolution ADF-STEM imaging. *Ultramicroscopy* **108**, 718–726 (2008).

35. H. G. Brown, R. Ishikawa, G. Sánchez-Santolino, N. R. Lugg, Y. Ikuhara, L. J. Allen, N. Shibata, A new method to detect and correct sample tilt in scanning transmission electron microscopy bright-field imaging. *Ultramicroscopy* **173**, 76–83 (2017).

36. G. Sághi-Szabó, R. E. Cohen, H. Krakauer, First-principles study of piezoelectricity in PbTiO₃. *Phys. Rev. Lett.* **80**, 4321–4324 (1998).

37. S. R. Zhang, Y. L. Zhu, Y. L. Tang, Y. Liu, S. Li, M. J. Han, J. Y. Ma, B. Wu, Z. H. Chen, S. Saremi, X. Ma, Giant polarization sustainability in ultrathin ferroelectric films stabilized by charge transfer. *Adv. Mater.* **29**, 1703543 (2017).

38. J. J. P. Peters, G. Apachitei, R. Beanland, M. Alexe, A. M. Sanchez, Polarization curling and flux closures in multiferroic tunnel junctions. *Nat. Commun.* **7**, 13484 (2016).

Science Advances

Subunit cell–level measurement of polarization in an individual polar vortex

Yuanwei Sun, Adeel Y. Abid, Congbing Tan, Chuanlai Ren, Mingqiang Li, Ning Li, Pan Chen, Yuehui Li, Jingmin Zhang, Xiangli Zhong, Jinbin Wang, Min Liao, Kaihui Liu, Xuedong Bai, Yichun Zhou, Dapeng Yu and Peng Gao

ARTICLE TOOLS	http://advances.sciencemag.org/content/5/11/eaav4355
SUPPLEMENTARY MATERIALS	http://advances.sciencemag.org/content/suppl/2019/10/25/5.11.eaav4355.DC1
REFERENCES	This article cites 38 articles, 4 of which you can access for free http://advances.sciencemag.org/content/5/11/eaav4355#BIBL
PERMISSIONS	http://www.sciencemag.org/help/reprints-and-permissions

Use of this article is subject to the Terms of Service